Applied Surface Science 592 (2022) 153327

Contents lists available at ScienceDirect

Applied Surface Science

journal homepage: www.elsevier.com/locate/apsusc

Full Length Article

Insights into the inherent properties of vertical graphene flakes towards hydrogen evolution reaction

Stefanos Chaitoglou [a,b,*], Roger Amade [a,b], Enric Bertran [a,b]

[a] Department of Applied Physics, Universitat de Barcelona, C/Martí i Franquès, 1, 08028 Barcelona, Catalunya, Spain
[b] ENPHOCAMAT Group, Institute of Nanoscience and Nanotechnology (IN2UB), Universitat de Barcelona, C/Martí i Franquès, 1, 08028 Barcelona, Catalunya, Spain

ARTICLE INFO

Keywords:
Graphene nanowalls
Plasma chemical vapor deposition
Hydrogen evolution

ABSTRACT

Nowadays, major research efforts are being carried out, in order to fulfil the demand for sustainable hydrogen production. To accelerate this process, it is important to develop efficient and inexpensive materials, going beyond precious metals and, if possible, using metal-free electrocatalysts. Carbon compounds could be an ideal candidate material, thanks to their abundancy in nature and the possibility to be organised in nanostructures with beneficial morphologies. Here, we report the deposition of vertical graphene flakes, otherwise known as graphene nanowalls (GNWs), in various metallic and non-metallic substrates and we present results on the inherent electrocatalytic activity towards hydrogen evolution reaction (HER) in acidic electrolyte. Analysis shows that when GNWs are deposited on top of an electrode with a higher inherent activity, overall activity is limited as GNWs block ion diffusion. When GNWs are deposited on electrodes with poorer activity, the inherent activity of GNWs is predominant. In addition, GNWs are successfully deposited on flexible electrodes and are applied to durability tests, including operation after manual bending, showing very good stability. Above all, the present study reports for first time the inherent electrocatalytic activity of GNWs towards HER. The results suggests that this carbon materials can be used in the development of novel catalysts.

1. Introduction

Hydrogen has attracted large attention during the last decade as it is considered a green and sustainable fuel, which is expected to play a major role towards the transition on the post-fossil fuels economy [1 2 3 4 5]. Nowadays, H_2 is mainly produced by i) natural gas steam reforming and ii) methanol reforming. Nevertheless, the first route is not based in a renewable energy source, while methane reforming results in the production of CO_2, which contributes to the greenhouse effect. Thus, the above routes are not sufficient to meet the energy demands of a post fossil fuel driven society while preventing global warming. Water splitting through electrolysis ($2H_2O \rightarrow 2H_2 + O_2$) is an environmentally responsible, carbon-free alternative technique for hydrogen generation. Water splitting takes place in an electrolytic cell (or electrolyzer) and requires a potential difference of 1.23 V to occur. The hydrogen evolution reaction (HER) and the oxygen evolution reaction (OER) occur at the cathode and the anode of the cell, producing gaseous hydrogen and oxygen molecules, respectively. Heterogeneous electrocatalysis is a process that can accelerate these electrochemical reactions on the surface of catalysts materials, promoting their initialization in lower potentials and under higher rates. For H_2 production, the design and development of efficient catalysts towards the HER is of fundamental importance.

Up today, noble metals of the platinum group (e.g. Rh, Pt, Ru) are the most attractive electrocatalysts for HER, as they possess low overpotentials, low Tafel slopes (the slope of a plot of the applied overpotential vs. the log10 of the resulting current density), high exchange current densities, and remarkable stabilities in water reduction reactions [6]. Nevertheless, the high cost and scarcity of these materials limit their potential application. The development of carbon-based electrocatalysts is a very promising alternative due to the abundant nature and low cost of carbon precursors. Thanks to their very high specific surface area, graphene and graphene derivatives can be applied in both energy harvesting and storage [7]. Up today, graphene and carbon nanotubes have been explored as electrocatalysts towards HER [8 9], while density funcional theory calculation have indicated the sharp edges of 3D graphene strucutres as the electrocatalytically active sites (see Supplementary Information Text 1). Moreover, apart from the contribution related to its inherent activity, graphene has been proven to improve charge transfer kinetics when applied as a coating on transition metal

* Corresponding author at: Department of Applied Physics, Universitat de Barcelona, C/Martí i Franquès, 1, 08028 Barcelona, Catalunya, Spain.
E-mail address: stefanoschaitoglou@ub.edu (S. Chaitoglou).

https://doi.org/10.1016/j.apsusc.2022.153327
Received 17 January 2022; Received in revised form 29 March 2022; Accepted 4 April 2022
Available online 11 April 2022

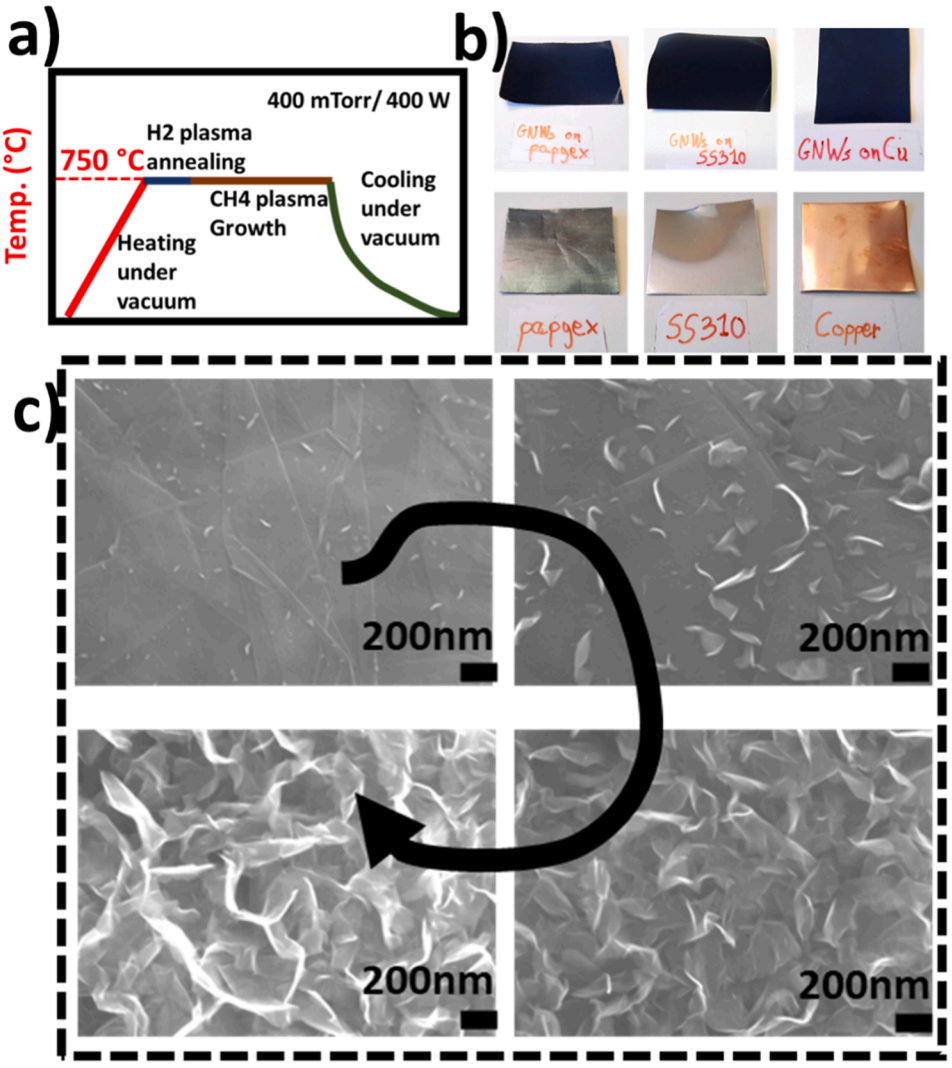

Fig. 1. a) drawing of the recipe for the GNWs growth, including the pre-treatment and synthesis steps, b) digital photographs of the Cu, SS and Papyex© substrates before and after the deposition of the GNWs film. By optical inspection the film appears similar to all three samples, c) sequence of SEM images showing the growth of GNWs over Papyex© in varying growth times (scale bar 200 nm), showing the evolution from the initial nucleation to complete coverage of the substrate. Arrow shows order of images based on increase of growth time.

carbide thin films [10 11].

Here, we report the synthesis of vertical graphene flakes (or graphene nanowalls), through inductively coupled plasma enhanced chemical vapor deposition. Differently from the growth of planar graphene, plasma conditions are required to promote the out of plane vertical growth of graphene flakes [12]. GNWs present the advantage of facile growth over both metallic and insulating substrates, while morphological features, e.g. thickness, height, density etc. can be controlled from the growth parameters. The GNWs function as a coating on one side of the growth substrates and tested as electrodes towards hydrogen evolution reaction in an acidic medium. Results show that the GNWs film can improve the inherent activity of poor-performing substrates, as well as operate with good endurance after being exposed to bending tests and a thousand of operation cycles.

2. Experimental part

2.1. Synthesis of graphene nano-walls (GNWs)

Graphene nano-walls were synthesized in 3 different substrates (310 Stainless steel foil, 100 μm thick, Ulbrich; polycrystalline copper foil, 99.9% pure, 100 μm thick, Basic Copper; Papyex© paper). All substrates were cut into pieces 35 × 50 mm, cleaned in an ultrasound bath of acetone and deionized water, and dried with a N_2 gun, before being inserted in the growth chamber. A graphite piece was used as a sample holder. The reactor is an inductively coupled plasma chemical vapor deposition (ICP-CVD) (13.56 MHz, power 440 W) system consisting of a long quartz tube (Vidrasa S.A., Ripollet, Spain) having a radio-frequency resonator (homemade), for producing remote plasma, and a tubular oven (PID Eng & Tech S.L., Madrid, Spain) working up to 1100 °C [13]. The sample was introduced in the oven, placed at a 30 cm distance from the plasma zone, and heated at 750 °C. The chamber was evacuated below 10^{-4} Pa with a turbomolecular pump. A short H_2 plasma is applied to clean and activate the surface. The H_2 plasma is produced by introducing 15 sccm (standard cubic centimeters per minute) of H_2 flow, for 5 min, at 400 mTorr and with an RF power of 400 W. GNWs are synthesized consecutively, by pausing H_2 and introducing 10 sccm of CH_4 (99.9% pure), under the same pressure and RF power conditions. Growth lasts 30 min. Then, CH_4 is paused and RF power and oven are turned off. Samples are cooled to room temperature (RT). A brief O_2 plasma (13 sccm of O_2, 0.5 min, 400 mTorr, 40 W RF power) is applied in RT to enhance the hydrophilicity of the GNWs, facilitating the electrochemical characterization, and the samples are consecutively removed from the tube.

2.2. Samples characterization

The morphology of the GNWs was in all substrates was observed by scanning electron microscopy (SEM) (JEOL JSM-7001F, operated at 15 kV, JEOL Ltd., Tokyo, Japan). The Image J software was used to measure

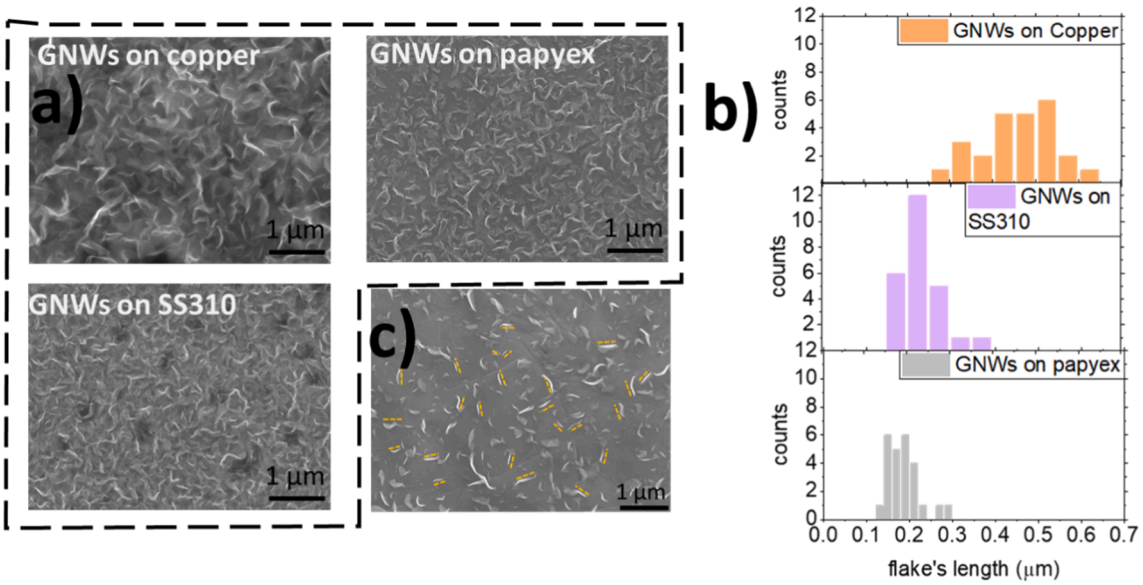

Fig. 2. a) SEM images showing the growth of GNWs film on Cu (upper left), Papyex© (upper right) and SS (down left) (scale bar is 1 μm), b) size distribution histogram of the GNWs over the different substrates (growth lasts 30′). c) SEM image of GNWs grown on Papyex© (scale bar is 1 μm). Yellow dotted lines show the orientation of various GNWs. (For interpretation of the references to colour in this figure legend, the reader is referred to the web version of this article.)

the length of the GNWs. XPS (X-ray photoelectron spectroscopy) experiments were performed in a PHI 5500 Multi-Technique System (Physical Electronics, Chanhassen, MN, USA) with a monochromatic X-ray source (Aluminium Kalfa line of 1486.6 eV energy and 350 W), placed perpendicular to the analyzer axis, and calibrated using the 3d5/2 line of Ag with a fullwidth at half maximum (FWHM) of 0.8 eV. The analyzed area was a circle of 0.8 mm diameter, and the selected resolution for the spectra was 187.5 eV of pass energy and 0.8 eV/step for the general spectra and 11.75 eV of pass energy and 0.1 eV/step for the spectra of the different elements. The vibrational modes of the samples were studied by Raman spectroscopy using a microscope HR800 (LabRam) (HORIBA France SAS, Palaiseau, France) with a 532 nm solid-state laser (5 mW laser power). The laser beam diameter is ~ 1 μm. 3 spectra were acquired from each sample and the average values of those were extracted for the relevant analysis. For x-ray diffraction measurements, it has been used a PANalytical XPert PRO MPD Bragg-Brentano powder diffractometer of 240 mm of radius. Samples were irradiated with a Co Ka radiation ($\lambda = 1.789$ Å), under 2θ scan from 2 to 80°, with step size of 0.017° and measuring time of 200 s per step. A Gaussian fitting was applied to extract the full width half maximum value (FWHM).

The electrochemical properties of the compounds were studied using a potentiostat/galvanostat (AutoLab, PGSTAT30, Eco Chemie B.V., Utrecht, The Netherlands). All experiments were carried out at room temperature in a typical three-electrode cell. An Ag/AgCl electrode (3 M KCl internal solution) and a graphite electrode were used as the reference and counter electrode, respectively. The working electrode was the sample of GNWs on the various growth substrates. The backside of the substrate was covered with an insulating tape. Linear sweep voltammetry (LSV) was employed with a scan rate of 5 mV s^{-1} in 0.5 M H_2SO_4 electrolyte. The LSV measurements were employed 8 times before recording the data, to ensure stability in electrode's performance. The electrodes endurance was evaluated by continuous cycling (1000 cycles) at a scan rate of 100 mV s^{-1} between − 700 and 0 mV (vs Ag/AgCl), as well as by chronoamperometry, employing a constant −0.41 V (vs RHE) and manual bending of the electrode for ~ 100 times. Charge transfer resistance was assessed by electrochemical impedance spectroscopy (EIS). A simple single-time constant equivalent circuit [R(RC)W] was used for interpolation of the measured EIS with the help of NOVA software. All potentials were recalculated with respect to a reversible hydrogen electrode (RHE).

3. Results and discussion

The sequence of steps for the nano-structures preparation is visualized in the illustration depicted in Fig. 1a. After removing from the oven, all samples have the same dark colour, as the GNWs film absorbs almost all light, thus the underlying substrate is no longer visible, as depicted in the sample's digital photographs before and after the GNWs deposition (Fig. 1b). Growth time in this series of samples was 30′. This is expected, as GNWs films have been estimated to absorb ~ 95% of light in a wide waveband from visible to near infrared [14]. The thickness of the GNWs film has been measured in previous work [15] and is estimated at ~ 1 μm.

We have studied in more detail the synthesis of the GNWs on the Papyex© substrate, varying the growth time between 5 and 60 min. Papyex© consists of graphitic crystals showing a preferred orientation together with a large non-oriented fraction. Thus, it is chemically stable, while it provides a high specific adsorption surface area, between 20 and 25 m^2/g [16]. The morphology of the Papyex© substrate can be observed in SEM image presented in Fig. 1c (upper-left figure). In this image, the initial nucleation of the GNWs is visible, after 2′ of growth time. In the sequence of SEM images, it can be observed the evolution in their growth with the pass of time, after5′ (upper-right figure), 30′ (down-right figure) and 60′ (down-left figure) of growth. GNWs reach a length ≥ 1 μm when growth lasts 60 min. Accordingly, the change in the colour of the sample from initial light grey (only Papyex© substrate) to very dark can be appreciated in the digital photo of samples presented in Fig. S1. A detailed description of the growth model of GNWs has been presented in another resent work by Baranov et al [17], in which it has been explained that ion bombardment is the driving force for the GNWs growth, as carbon species are supplied through surface diffusion but not directly from the gas phase. Thus, growth velocity is not constant but declines with time, meanwhile nucleation of GNWs is considered to depend on the generation of a large number of ion-induced defects on the surface of the substrate.

Next, we describe the findings resulting from the growth on Cu, stainless steel and Papyex©, under the same growth conditions (see experimental section). Growth lasted 30 min, as it has been estimated to be the required time in order to achieve a homogeneous coverage of the substrate with the GNWs film. The morphology of the GNWs in each substrate can be observed in Fig. 2a. The GNWs deposited over Cu

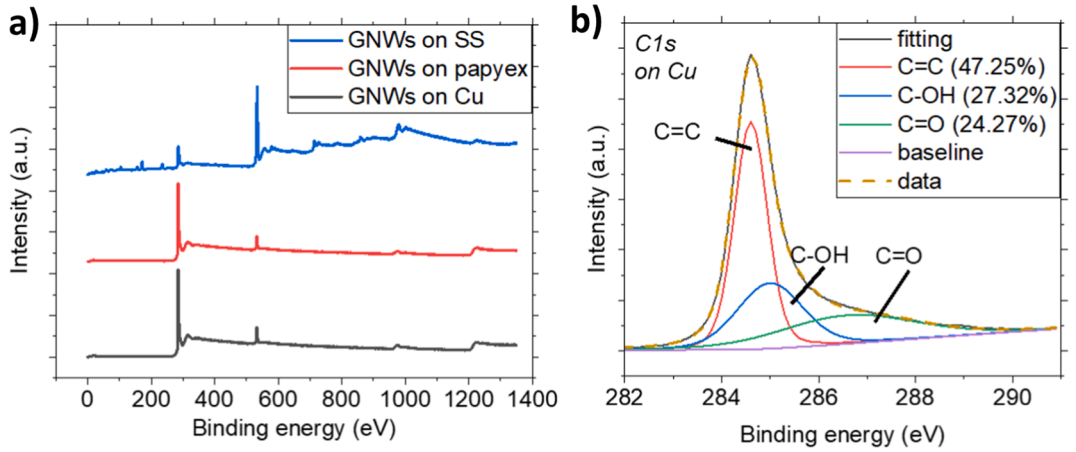

Fig. 3. a) XPS broad scan spectra of GNWs on three different substrates. Spectra of GNWs on Cu (black graph) and Papyex© (red graph) reveal presence of carbon and oxygen. Spectrum of GNWs on SS (blue graph) reveals additionally presence of Fe, Al, Cr, Si and S, originating from the substrate. b) XPS analysis of the GNWs /Cu electrode and analysis of high-resolution C 1 s spectrum of the GNWs. (For interpretation of the references to colour in this figure legend, the reader is referred to the web version of this article.)

appear to be longer, in comparison to those over Papyex© and stainless steel. We measured the length of the flakes and present the results on a histogram of the size distribution (Fig. 2b). Indeed, flakes over Cu are larger (~0.4–0.6 μm), in comparison to those over SS (~0.22–0.4 μm) and those over Papyex© (~0.05–0.3 μm). Similar trends are observed in GNWs deposited in shorter growth time (8′) in all three substrates (Fig. S2). These results can be explained by taking into consideration the possible co-catalytic effects of the substrates. Metallic Cu and SS are well-known catalytic substrates [18 19] that promote graphene growth in CVD processes, thus it is foreseen that they can promote the faster growth of GNWs, in comparison to Papyex©. Between the two firsts, Cu is known to promote the growth of single layer graphene. This is attributed to the very low C species solubility into bulk Cu. Thus, growth is self-limited once the first layer is formed [20]. SS, on the other hand,

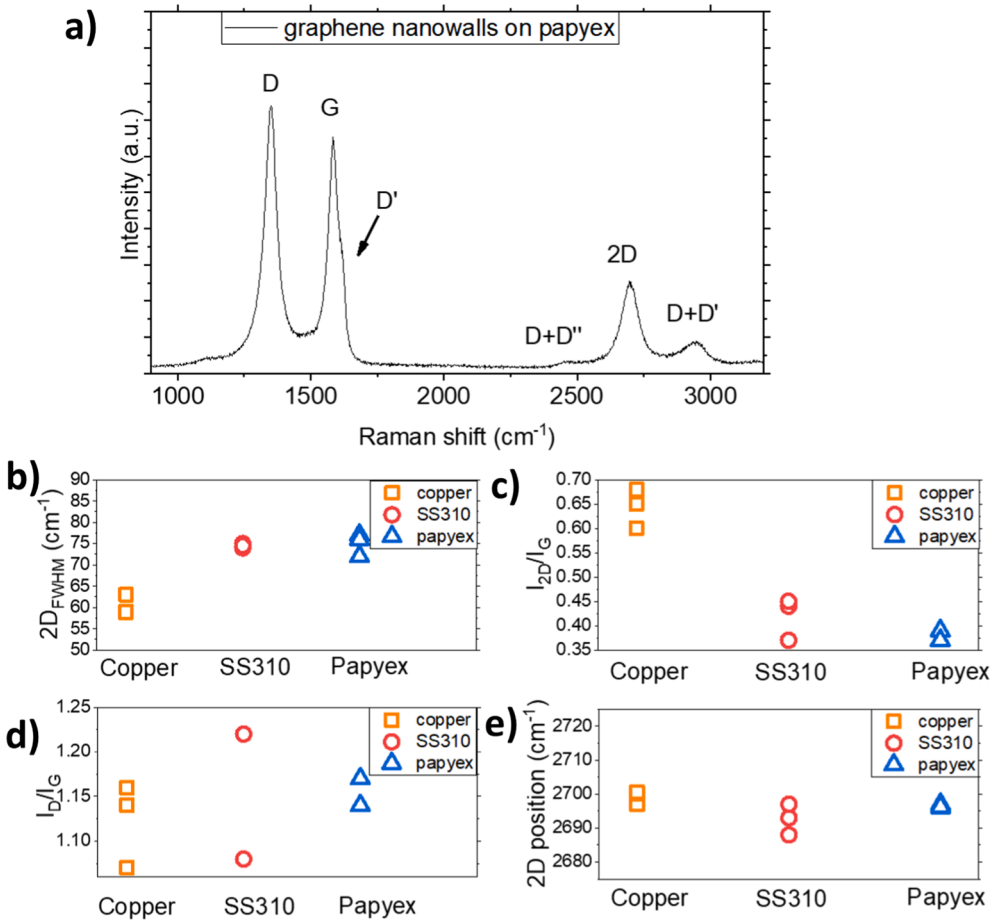

Fig. 4. a) Raman spectrum of the GNWs/ Papyex© electrode, in which all the main graphene bands are depicted, b) data of the $FWHM_{2D}$, c) data of the I_{2D}/I_G, d) data of the I_D/I_G, e) data of exact position of the 2D band, for graphene deposited in three different substrates.

contains Fe, Cr, Ni, and Mn, elements in which C species are soluble. Thus, we consider that more C species remain available on the Cu surface during ion bombardment, which explains the higher growth rate in comparison to growth on the SS surface.

Finally, in Fig. 2c we observe the nuclei of GNWs after 5′ synthesis. Dotted yellow lines are used to mark the orientation of various GNWs. It is observed that these do not exhibit any preferred orientation. Moreover, bending of the GNWs is observed in various cases (Fig. 1c and Fig. 2a). This feature further differentiates the growth of vertical graphene from this of planar graphene, whose orientation depends on the crystallographic orientation of the underlying substrate [21].

XPS characterization was performed in order to obtain further information regarding the GNWs composition. The wide scans for three samples are presented in Fig. 3a. Spectra of GNWs on Cu (black graph) and Papyex© (red graph) reveal the presence of carbon and oxygen. Spectrum of GNWs on SS (blue graph) further reveals the presence of Fe, Al, Cr, Si and S, originating from the substrate. High resolution XPS analysis has been carried out to detect information about the bonding states in the GNWs/ Cu electrode. Deconvoluted C 1 s spectra revealed the presence of three components centred at 284.6, 284.9 and 286.6 eV attributed, respectively, to C = C sp^2, C − OH (hydroxyl) and C = O (Fig. 3b). The areal percentage of each component is 47.25%, 27.32% and 24.27%, respectively. The high amount of C-OH and C = O bonds make evident the defective crystal nature of the graphene nanostructure, a fact that is further supported by Raman spectroscopy data that we will show below. Oxygen contamination may originate to the reaction with ambient oxygen and moisture once exposed to ambient conditions [13]. High resolution spectra of the C1s peaks for each sample are presented in Fig. S3a. The variation with respect to the position and the shape between the peaks reveals differences in the composition. Detailed deconvoluted peaks of GNWs on SS and Papyex© are presented in Fig. S3b. The results regarding the % concentration and position of each peak are presented in Table S1. We highlight the change in the % concentration of C-OH and C = O bonds between the different samples, which shows the variation in the concentration of defects in the GNWs. Specifically, the GNWs on Papyex© show a concentration of C OH bonds of 31.32%, higher than that of GNWs on Cu (27.32%) and lower than this of GNWs on SS (38.67%).

Raman spectroscopy characterization was performed on all 3 samples to study the crystal quality and morphology of the GNWs. A typical Raman spectrum is presented in Fig. 4a. The main features of the spectrum are the bands centred at 1351.4 cm^{-1} (D peak), at 1582.7 cm^{-1} (G peak) and at 2701 cm^{-1} (2D peak). D band is related to the presence of structural defects, vacancies, boundaries, etc that are present in the graphene crystal and activate the breathing mode of hexagonal carbon rings. On the other hand, the G band corresponds to the doubly degenerate E_{2g} phonon at the Brillouin-zone center. The 2D band is the second order of the D band and is manifested in a single peak in monolayer graphene, whereas it splits in four bands in bilayer graphene [22]. Other minor bands are centred at 1616 cm^{-1} (D', manifested as a right shoulder on the G band and associated with finite-size graphite crystals and graphene edges [23]), at 2466 cm^{-1} (D + D'') and at 2949 cm^{-1} (D + D', related to sp^2 CH stretching vibrations). By analysis of the main bands, we extract the following information. The full width half maximum of the 2D band provides information regarding the number of graphene layers attached between them by Van der Waals forces (Fig. 4b). In our samples, in GNWs deposited on Cu, the $FWHM_{2D}$ takes an average value of 60.3 cm^{-1}, in GNWs deposited on SS it takes an average value of 74.5 cm^{-1}, and in GNWs deposited on Papyex© it takes an average value of 75 cm^{-1}. Thus, GNWs over copper consist on average of about ~ 3–4 graphene single layers [24], while GNWs over SS and Papyex© consist of more layers (~7–8), nevertheless without resembling the spectra of graphite [25]. The I_{2D}/I_G ratio values confirm the above observations, as the ratio for GNWs on Cu is higher (~0.64) than those on SS and Papyex© (0.42 and 0.37 respectively), manifesting the thinner morphology of the first [26] (Fig. 4c). Structural defects can

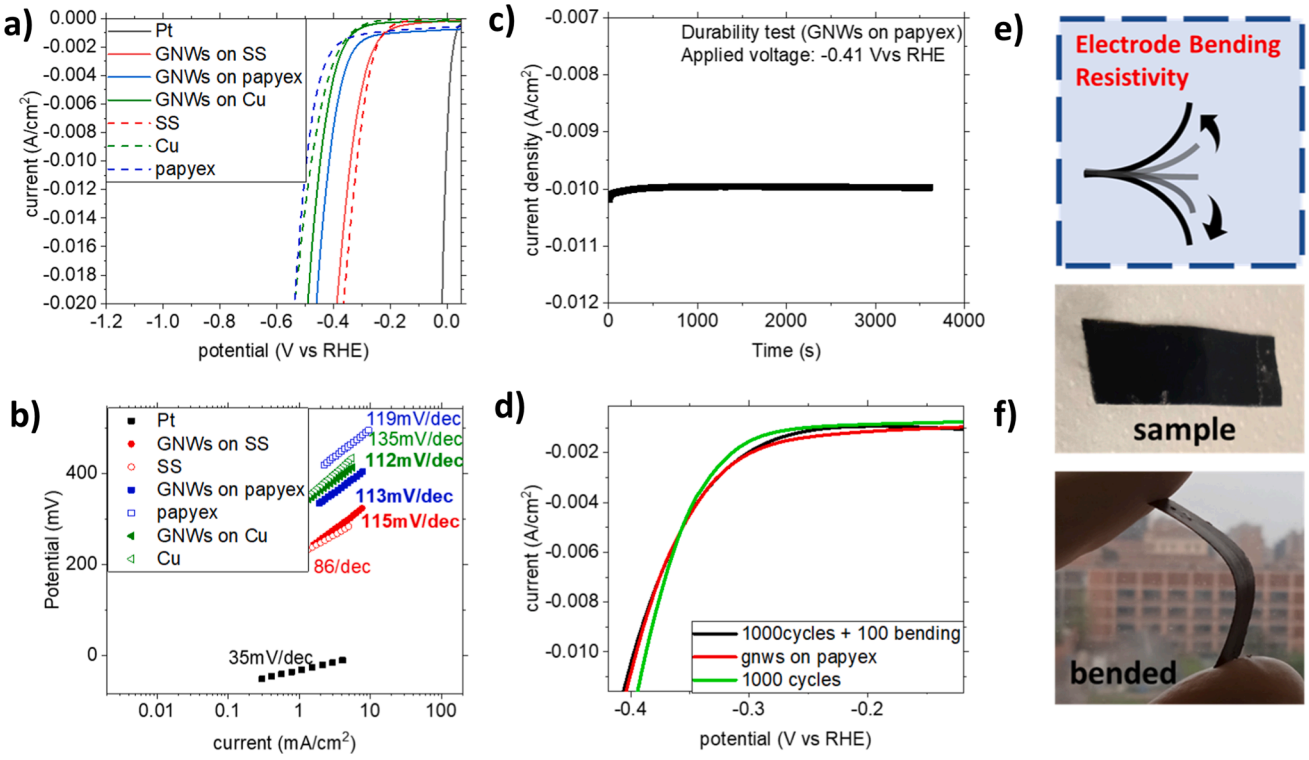

Fig. 5. a) Graph with LSV curves of bare electrodes and electrodes with GNWs coating on top, b) Graph with Tafel slopes of all electrodes tested with LSV (slope values in bold correspond to the GNWs on substrate, for each electrode), c) graph with chronoamperometry test applied to the GNWs/Papyex© electrode during 1 h, d) graph with LSV curves of as-prepared GNWs/Papyex© electrode before and after exposed to durability tests, including manual bending and operation after 1,000 cycles of operation, e) drawing of the electrode depicting bending experiment and f) photographs of the bended electrode.

be evaluated by measuring the I_D/I_G ratio. For GNWs over Cu, this ratio is 1.12, while for GNWs over SS and Papyex© it is 1.12 and 1.16, respectively (Fig. 4d). It appears that structural defects on GNWs are not related to the growth substrate. To quantitate the number of defects, we take the profit of [27] the analysis made by Tuinstra and Koenig and the more recent expressions reported by Ferrari and Cancado [28]. According to these works, we can use Eq. (1).

$$L_D^2(nm^2) = (1.8 \pm 0.5)x10^{-9}\lambda_L^4\left(\frac{I_D}{I_G}\right)^{-1} \quad (1)$$

where λ_L is the excitation laser wavelength in nm (532 nm) and calculate the distance L_D (in nm) between two point-defects. Inter-defect distance is calculated ~ 11.3 nm (for GNWs on Cu and SS) and 11.1 nm (for GNWs on Papyex©). The density of defects per area can be calculated through equation (2).

$$n_D(cm^2) = \frac{(1.8 \pm 0.5)x10^{22}}{\lambda_L^4}\left(\frac{I_D}{I_G}\right) \quad (2)$$

Thus, the quantity of defects n_D in the crystal lattice depends linearly from the $\frac{I_D}{I_G}$ ratio. In the electrodes, defects are present with a density ~ 2.5×10^{11} /cm^2 (for GNWs on Cu and SS) and ~ 2.7×10^{11} /cm^2 (for GNWs on Papyex©) in the crystal lattice, which is an importantly increased amount, especially if compared with the density of defects usually present in planar few layers graphene films prepared by CVD [29]. Probably, the morphology of the GNWs (high amount of lateral grain boundaries, growth occurring during continuous ion bombardment) accounts for the high density of defects. Nevertheless, it needs to be evaluated how these defects affect the electrocatalytic properties of the GNWs. The positions of the 2D bands are located at 2699.1, 2692.6 and 2696.4 cm^{-1} for the GNWs grown on Cu, SS and Papyex©, respectively (Fig. 4e). Such shifts in the phonon frequencies are attributed to changes in the dimension of the crystal lattice, which can lead to changes of the inherent strain in the GNWs. The amount of strain can be calculated using the Grüneisen parameter γ_D (adimensional) whose value has been previously calculated experimentally to be 3.55 for graphene and apply the Eq. (3).

$$\varepsilon = -\frac{\Delta u_{2D}}{2u_{2D}^0\gamma_D} \quad (3)$$

where Δu_{2D} denotes the shift of the frequency of the 2D phonon mode with respect to $u_{2D}^0 = 2680$ cm^{-1}, the frequency of the 2D mode of unstrained pristine graphene [30]. The calculation of strain of GNWs provided similar values of compressive stress, ε = -0.1%, −0.06% and −0.08% over Cu, SS and Papyex©, respectively, which remain within the range –0.08%±0.02%. The vertical growth of GNWs discards strain related to lattice mismatch between graphene and substrate, therefore strain should be mostly related to the bended nature of the GNWs, as this can be appreciated in the microscopy images (Fig. 1). The Raman spectra used for the analysis presented in Fig. 4b-e are presented in Fig. S4.

XRD characterization was used to obtain more information about the crystal structure of the GNWs deposited on Cu. The (0 0 2) graphene peak is observed at 30.35° (Fig. S5). The peak has a FWHM of 1.95°. According to the analysis performed in [31], based on the use of Scherrer's equation, we calculated that GNWs consist of ~ 5 layers, which is consistent with the results arising from the Raman analysis.

The electrocatalytic properties and durability of the GNWs towards HER were evaluated by LSV and chronoamperometry for samples deposited in all substrates. Fig. 5a shows the polarization curves of Pt foil, GNWs/Cu, GNWs/SS, GNWs/Papyex© (solid lines) and the substrates only (interrupted lines), after being annealed in high temperature in a H_2 plasma atmosphere (to reproduce the cleaning and activation process applied prior to GNWs deposition). Pt foil shows an onset potential of 0 V and an overpotential of 34 mV when −10 mA/cm^2 are generated. This current value is used as a reference as it is the approximate current density expected for a 10% efficient solar-to-fuels conversion device under one sun illumination, thus it is widely used in literature to compare the efficiency of both electrocatalysts and photocatalysts. Meanwhile, the Tafel slope value for the Pt foil is 34 mV/dec (Fig. 5b). Both above values are in agreement with literature, for Pt [31]. SS electrode displays an onset potential at −192 mV and an overpotential at −10 mA/cm^2 of –320 mV. The corresponding values for the GNWs/SS electrode are –178 mV (onset potential) and –340 mV (overpotential). Thus, the GNWs film promotes the faster evolution of the hydrogen reaction, as manifested in the reduced onset potential value, while it later limits the reactions (manifested in the increased overpotential value). These finding are correlated with the fact that the inherent catalytic properties of GNWs are poorer compared to those of SS, which is composed of metallic elements which are good electrocatalysts (e.g. Ni, see Energy-Dispersive spectrum in Fig. S6). Pristine graphene films have been reported before to serve as atomic barriers over metallic substrates, blocking the diffusion of ions towards the surface of the metallic electrode [9]. The reduced onset potential value can be explained taking into consideration the hydrophilic nature of the GNWs. The sluggier kinetics are manifested in the Tafel slope values as well, in which SS manifest a value of 86 mV/dec, while the GNWs/SS manifest a value of 115 mV/dec. Therefore, it appears that the GNWs film does not improve the electrocatalytic performance SS, when applied as a coating on the substrate. This observation is opposite to what has been reported in many works regarding the application of pristine single layer graphene over catalytic surfaces. In many works it has been exhibited that graphene improved the inherent electrocatalytic properties of 2D and nanostructured materials, when applied as a coating on their surface [32,33]. Of course, despite the similar crystal structure, GNWs differ from graphene in terms of thickness and morphology, therefore differences in the electrocatalytic response are justified. In the case of Cu and Papyex©, when GNWs are applied on top, the electrocatalytic performance improves. In concrete, the onset potential of bare Cu is 20 mV higher that this of the GNWs/ Cu (−303 mV and −283 mV, respectively), while the overpotential value decreases ~ 40 mV (−480 mV for bare Cu and −440 mV for GNWs/Cu). Moreover, Tafel slope value reduces from 135 mV/dec for bare Cu to 112 mV/dec for GNWs/Cu. Similar results were obtained in the case of GNWs over Papyex©. In concrete, the onset potential of bare Papyex© is 40 mV higher that this of the GNWs/Papyex© (−260 mV and −220 mV, respectively), while the overpotential value decreases ~ 90 mV (−500 mV for bare Papyex© and −410 mV for GNWs/Papyex©). Moreover, Tafel slope value reduces from 119 mV/dec for bare Papyex© to 113 mV/dec for GNWs/Papyex©. These results demonstrate that when the GNWs film is applied on a surface of a poor catalytic material, the electrode can operate in a more efficient way thanks to the inherent performance of the GNWs. The comparison between GNWs on Cu and GNWs on Papyex© shows a slightly better activity of the second. This may be related with the fact that GNWs on Papyex© possess more structural defects and its wall is formed from more atomic layers, according to the XPS and Raman analysis provided above. Overall, electrocatalytic activity and defect concertation follow the same trend between the three samples. Nevertheless, more results are required in order to confirm this hypothesis. Despite the fact that pristine graphene is widely considered as inert towards the HER, the peculiar morphology and moderate defect density present in the GNWs, altogether with the very high specific surface area per electrode surface, increase the electrocatalytic performance of the latest.

Various durability tests are performed in continuation to further evaluate the performance of the GNWs/Papyex© electrode. We use the Papyex© substrate for the durability tests, as it is more flexible, compared to Cu and SS, and chemically inert, therefore it is suitable for the chronoamperometry and cycling experiments. First, chronoamperometry is applied to evaluate the endurance of the electrode (Fig. 5c). The current density remains stable during 3600 s of operation

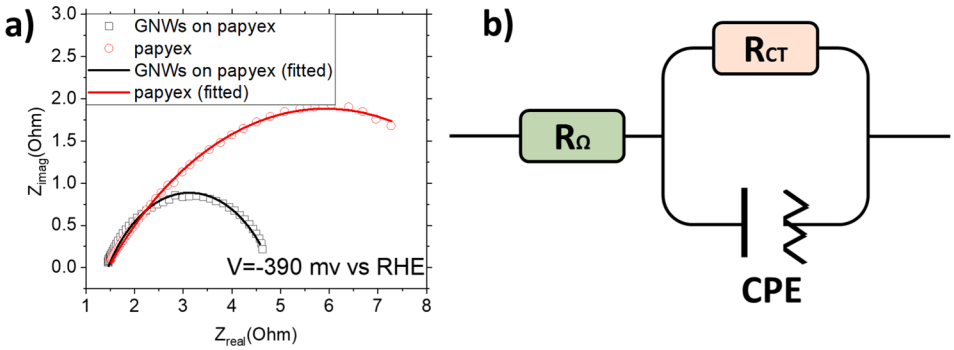

Fig. 6. a) Nyquist plots of the GNWs on Papyex© and pristine Papyex© electrode recorded at 390 mV vs RHE. Both experimental data and fitted data are exhibited. b) equivalent circuit used for data fitting;

Table 1
Equivalent circuit parameters obtained from fitting the EIS data of GNWs on Papyex© and Papyex© substrate.

Electrode material	R_Ω (Ω)	R_{CT} (Ω)	$Z_Q = 1/[Q_0(j\omega)^n]$ Q_0 ($\Omega^{-1}\cdot s^{-n}$)	n
Papyex® paper	1.73	8.82	0.026	0.51
GNWs on Papyex® paper	1.45	3.35	0.011	0.62

under a stable potential of –0.41 V (vs RHE). A stable current density of -10 mA/cm^2 is produced, which is in agreement with the results of LSV (Fig. 5a). We additionally performed durability test over 1000 voltammetry cycles, and the HER activity of the GNWs/Papyex© electrode after this load is displayed in Fig. 5d (green line). Comparison with the electrode's activity before cycling (red line) shows a negligible performance drop, proving the very long durability and chemical stability properties of the GNWs nanostructures. Finally, the electrode was exposed to bending test, to evaluate its mechanical stability. The electrode was bended up and downwards, as illustrated in the draw in Fig. 5e. The flexible nature of the Papyex© substrate can be appreciated in the photos shown in Fig. 5f. The electrode has a very good stability after 100 bending cycles (performed manually), as no changes in the polarization curve are observed (Fig. 5d, black line). The very good mechanical stability indicates the potentiality of the GNWs/Papyex© electrode to be used in flexible electronic devices [34].

The Nyquist plots obtained from the EIS on the GNWs/Papyex© and Papyex© bare electrode are presented in Fig. 6a. Only one semicircle appears for both electrodes over the explored frequency range (from 100 kHz to 1 Hz), which indicates that the charge transfer process is the principal reaction on the catalysts' surface. EIS is performed at the overpotential regime for both electrodes (−390 V vs RHE). The equivalent circuit used for fitting the measurement results is included in the inset to Fig. 6b. It consists of combined resistance (R_Ω), usually ascribed to resistance of electrolyte and electrode material, connected in series with a parallel arrangement of the constant phase element (CPE) and the charge transfer resistance (R_{ct}), related to chemical processes at the electrode/electrolyte interface opposing the flow of charge carriers that participate in HER The R_{ct} can be approximately estimated by the semicircle diameter, thus the bare Papyex© electrode has a R_{ct} of 8.9 Ω, while the GNWs/Papyex© electrode has a Rct of 3.35 Ω. Both experimental values (points) are in agreement with those calculated by the fitting procedure (lines) (Fig. 6a and Table 1). The capacitance related to CPE is slightly higher for the Papyex© sample, which corresponds with a higher charge transfer resistance. Concluding, the EIS responses validate the HER performances of the studied catalysts. Comparison of the cyclic voltammetry curves of bare Papyex© and GNWs on Papyex© showed a 6-fold enhancement for the latest (Fig. S7), indicating that the enhanced HER activity might originate from the increased electrochemical active area.

Compared to noble metal-based catalysts, the HER activity of the GNWs is lower. For noble metals, the onset potential values are 0 V and the Tafel slope is ~ 30 mV/dec, Therefore, tenths of mA/cm^2 are generated at overpotentials < 0.1 V [35]. Ultimately, to enhance the inherent HER activity of GNWs and approach the activity of noble metals, other routes to increase the number of active sites should be explored.

4. Conclusions

GNWs are the vertical derivative of 2-dimensional graphene. Here, we have demonstrated the growth of GNWs in a variety of metallic and non-metallic substrates and provide insights on their morphology and crystalline quality. The inherent properties of the GNWs towards HER in acidic medium have been evaluated for all substrates. The findings reveal that when the substrate has higher quality as electrocatalyst than the GNWs film, its activity becomes limited due to the deposition of the GNWs coating which acts as a barrier. Only when the substrate has a lower quality as electrocatalyst than the GNWs, the performance of the electrode resembles this of the GNWs coating. Moreover, the GNWs deposited on flexible Papyex© demonstrate very high endurance properties after one thousand cycles of operation and after being exposed to manual bending. These findings are expected to carry forward the research towards development of metal-free electrocatalytic electrodes, which can potentially replace rare or noble metals in many practical applications.

CRediT authorship contribution statement

Stefanos Chaitoglou: Conceptualization, Methodology, Formal analysis, Investigation, Writing – original draft, Writing – review & editing. **Roger Amade:** Methodology, Investigation, Writing – original draft, Writing – review & editing. **Enric Bertran:** Resources, Writing – original draft, Writing – review & editing.

Declaration of Competing Interest

The authors declare that they have no known competing financial interests or personal relationships that could have appeared to influence the work reported in this paper.

Acknowledgements

The authors acknowledge the support of CCiT-UB for electronic microscopy aids and spectroscopic measurements. SC acknowledge the help of Dr. Xavier Alcobe on the interpretation of the XRD results. It is acknowledged financial support of the Spanish Ministry of Economy, Industry and Competitiveness (MINECO) under Project Nos. ENE2017-89210-C2-2-R, and PID2020-116612RB-C32, and support from the

AGAUR of , through Project No. . S.C. acknowledges support from the postdoctoral fellowhips programme Beatriu de Pinós, funded by the Secretary of Universities and Research (Government of Catalonia) and by the Horizon 2020 programme of research and innovation of the European Union under the Marie Sklodowska-Curie grant agreement No (H2020-MSCA-COFUND-2017).

Appendix A. Supplementary data

Supplementary data to this article can be found online at https://doi.org/10.1016/j.apsusc.2022.153327.

References

[1] I. Roger, M.A. Shipman, M.D. Symes, Earth-abundant catalysts for electrochemical and photoelectrochemical water splitting, Nat. Rev. Chem. 1 (1) (2017), https://doi.org/10.1038/s41570-016-0003.
[2] G. Glenk, S. Reichelstein, Economics of converting renewable power to hydrogen, Nat. Energy 4 (2019) 216–222, https://doi.org/10.1038/s41560-019-0326-1.
[3] S. Zhang, G. Gao, H. Zhu, L. Cai, X. Jiang, S. Lu, F. Duan, W. Dong, Y. Chai, M., Du *In situ interfacial engineering of nickel tungsten carbide Janus structures for highly efficient overall water splitting*, Science Bulletin 65 (2020) 640–650, https://doi.org/10.1016/j.scib.2020.02.003.
[4] Z. Zhu, J. Hao, H. Zhu, S. Sun, F. Duan, S. Lu, M. Du, In situ fabrication of electrospun carbon nanofibers-binary metal sulfides as freestanding electrode for electrocatalytic water splitting, Adv. Fiber Mater. 3 (2) (2021) 117–127, https://doi.org/10.1007/s42765-020-00063-7.
[5] H. Zhu, L.i. Gu, D. Yu, Y. Sun, M. Wan, M. Zhang, L. Wang, L. Wang, W. Wu, J. Yao, M. Du, S. Guo, The marriage and integration of nanostructures with different dimensions for synergistic electrocatalysis, Energy Environ. Sci. 10 (1) (2017) 321–330, https://doi.org/10.1039/C6EE03054H.
[6] Z. Chen, X. Duan, W. Wei, S. Wang, B.-J. Ni, Recent advances in transition metal-based electrocatalysts for alkaline hydrogen evolution, J. Mater. Chem. A 7 (25) (2019) 14971–15005.
[7] S. Chaitoglou, R. Amade, E. Bertran, Evaluation of graphene/WO3 and graphene/CeO x structures as electrodes for supercapacitor applications, Nanoscale Res. Lett. 12 (1) (2017), https://doi.org/10.1186/s11671-017-2385-1.
[8] T. Li, C. Wang, Y. Li, Y. Wu, C. Li, X. Zhang, F. Yang, Orientated carbon nanotubes boosting faster charge transfer for bifunctional HER and OER, Int. J. Hydrog. Energy 46 (2021) 1904–1912, https://doi.org/10.1016/j.ijhydene.2020.10.017.
[9] A. Xie, N. Xuan, K. Ba, Z. Sun, Pristine graphene electrode in hydrogen evolution reaction, ACS Appl. Mater. Interfaces 9 (5) (2017) 4643–4648, https://doi.org/10.1021/acsami.6b14732.
[10] S. Chaitoglou, T. Giannakopoulou, T. Speliotis, A. Vavouliotis, C. Trapalis, A. Dimoulas, Mo 2 C/graphene heterostructures: low temperature chemical vapor deposition on liquid bimetallic Sn–Cu and hydrogen evolution reaction electrocatalytic properties, Nanotechnology 30 (12) (2019) 125401, https://doi.org/10.1088/1361-6528/aaf9e8.
[11] D. Geng, X. Zhao, Z. Chen, W. Sun, W. Fu, J. Chen, W. Liu, W. Zhou, K.P. Loh, Direct synthesis of large-area 2D Mo 2 C on in situ grown graphene, Adv. Mater. 29 (35) (2017) 1700072, https://doi.org/10.1002/adma.201700072.
[12] K. Davami, M. Shaygan, N. Kheirabi, J. Zhao, D.A. Kovalenko, M.H. Rummeli, J. Opitz, G. Cuniberti, J.S. Lee, M. Meyyappan, Synthesis and characterization of carbon nanowalls on different substrates by radio frequency plasma enhanced chemical vapor deposition, Carbon 72 (2014) 372–380, https://doi.org/10.1016/j.carbon.2014.02.025.
[13] A. Musheghyan-Avetisyan, F. Güell, P.R. Martínez-Alanis, R. Amade, J. Martí-González, E. Bertran-Serra, Photoluminescence from carbon structures grown by inductively coupled plasma chemical vapor deposition, J. Vac. Sci. Technol., A 38 (2) (2020) 023405, https://doi.org/10.1116/1.5140415.
[14] J. Nong, W.Wei, X. Song, L. Tang, J. Yang, T. Sun, L. Yu, W. Luo, C. Li, D. Wei, Direct growth of graphene nanowalls on silica for high-performance photo-electrochemical anode, Surf. Coat. Technol., 320 (2017) 579-583; DOI: 10.1016/j.surfcoat.2016.10.092.
[15] Y. Esqueda-Barrón, A. Pérez del Pino, P.G. Lebière, A. Musheghyan-Avetisyan, E. Bertran-Serra, E. György, C. Logofatu, Boost of charge storage performance of graphene nanowall electrodes by laser-induced crystallization of metal oxide nanostructures, ACS Appl. Mater. Interfaces 13 (15) (2021) 17957–17970, https://doi.org/10.1021/acsami.1c00951.
[16] Y. Finkelstein, D. Nemirovsky, R. Moreh, G. Kimmel, Study of the Papyex structure using neutron Compton scattering, Phys. B 291 (1-2) (2000) 213–218, https://doi.org/10.1016/S0921-4526(99)01876-1.
[17] O. Baranov, I. Levchenko, S. Xu, J.W.M. Lim, U. Cvelbar, K. Bazaka, Formation of vertically oriented graphenes: what are the key drivers of growth? 2D Mater., 5 (2018) 044002; DOI; 10.1088/2053-1583/aad2bc.
[18] S. Chaitoglou, E. Bertran, Effect of pressure and hydrogen flow in nucleation density and morphology of graphene bidimensional crystals, Mater. Res. Express, 3 (2016) 075603; DOI: 10.1088/2053-1591/3/7/075603.
[19] R. John, A. Ashokreddy, C. Vijayan, T. Pradeep, Single- and few-layer graphene growth on stainless steel substrates by direct thermal chemical vapor deposition, Nanotechnology, 22 (2011) 165701; DOI: 10.1088/0957-4484/22/16/165701.
[20] S. Chaitoglou, E. Bertran, Effect of temperature on graphene grown by chemical vapor deposition, J. Mater. Sci. 52 (2017) 8348–8356, https://doi.org/10.1007/s10853-017-1054-1.
[21] E. Meca, J. Lowengrub, H. Kim, C. Mattevi, V.B. Shenoy, Epitaxial graphene growth and shape dynamics on copper: phase-field modeling and experiments, Nano Lett. 13 (2013) 5692–5697, https://doi.org/10.1021/nl4033928.
[22] T.M.G. Mohiuddin, A. Lombardo, R.R. Nair, A. Bonetti, G. Savini, R. Jalil, N. Bonini, D.M. Basko, C. Galiotis, N. Marzari, K.S. Novoselov, A.K. Geim, A.C. Ferrari, Uniaxial strain in graphene by Raman spectroscopy: G peak splitting, Grüneisen parameters,and sample orientation, Phys. Rev. B, 79 (2009) 205433; DOI: 10.1103/PhysRevB.79.205433.
[23] T. Mori, M. Hiramatsu, K. Yamakawa, K. Takeda, M. Hori, Fabrication of carbon nanowalls using electron beam excited plasma-enhanced chemical vapor deposition, Diam. Relat. Mater. 17 (7-10) (2008) 1513–1517, https://doi.org/10.1016/j.diamond.2008.01.070.
[24] V.L. Nguyen, D.L. Duong, S.H. Lee, J. Avila, G. Han, Y.-M. Kim, M.C. Asensio, S.-Y. Jeong, Y.H. Lee, Layer-controlled single-crystalline graphene film with stacking order via Cu–Si alloy formation, Nat. Nanotechnol. 15 (10) (2020) 861–867, https://doi.org/10.1038/s41565-020-0743-0.
[25] M.M. Bernal, E.M. Perez, One-pot exfoliation of graphite and synthesis of nanographene/dimesitylporphyrin hybrids, Int. J. Mol. Sci. 16 (2015) 10704–10714, https://doi.org/10.3390/ijms160510704.
[26] I. Calizo, I. Bejenari, M. Rahman, G. Liu, A.A. Balandin, Ultraviolet Raman microscopy of single and multilayer graphene, J. Appl. Phys. 106 (4) (2009) 043509, https://doi.org/10.1063/1.3197065.
[27] F. Tuinstra, J.L. Koenig, Raman spectrum of graphite, J. Phys. Chem. 5 (1970) 1126–1130, https://doi.org/10.1063/1.1674108.
[28] L.G. Cancado, A. Jorio, E.H. Martins Ferreira, F. Stavale, C.A. Achete, R.B. Capaz, M.V.O. Moutinho, A. Lombardo, T.S. Kulmala, A.C. Ferrari, Quantifying defects in graphene via Raman spectroscopy at different excitation energies, Nano Lett. 11 (2011) 3190–3196, https://doi.org/10.1021/nl201432g.
[29] S. Chaitoglou, E. Bertran, Control of the strain in chemical vapor deposition-grown graphene over copper via H 2 flow, J. Phys. Chem. C 120 (44) (2016) 25572–25577.
[30] G.V. Troppenz, M.A. Gluba, M. Kraft, J. Rappich, N.H. Nickel, Strain relaxation in graphene grown by chemical vapor deposition, J. Appl. Phys. 114 (21) (2013) 214312, https://doi.org/10.1063/1.4834538.
[31] S.H. Huh, X-ray diffraction of multi-layer graphenes: Instant measurement and determination of the number of layers, Carbon 78 (2014) 617–621.
[32] S. Chaitoglou, T. Giannakopoulou, D. Tsoutsou, A. Vavouliotis, C. Trapalis, A. Dimoulas, Direct versus reverse vertical two-dimensional Mo 2 C/graphene heterostructures for enhanced hydrogen evolution reaction electrocatalysis, Nanotechnology 30 (41) (2019) 415404, https://doi.org/10.1088/1361-6528/ab3155.
[33] S. Chaitoglou, T. Giannakopoulou, G. Papanastasiou, D. Tsoutsou, A. Vavouliotis, C. Trapalis, A. Dimoulas, Cu vapor-assisted formation of nanostructured Mo2C electrocatalysts via direct chemical conversion of Mo surface for efficient hydrogen evolution reaction applications, Appl. Surf. Sci. 510 (2020) 145516, https://doi.org/10.1016/j.apsusc.2020.145516.
[34] Z. Chen, X. Guo, Y. Liu, W. Zhang, X. Tang, Y. Zheng, Y. Wang, L. Li, Z. Wang, Y. Zhao, Facile preparation of graphene nanowalls/EVA hybrid film for ultraflexible transparent electrodes, J. Solid State Electrochem. 23 (2019) 1473–1480, https://doi.org/10.1007/s10008-019-04231-7.
[35] N. Cheng, S. Stambula, D.a. Wang, M.N. Banis, J. Liu, A. Riese, B. Xiao, R. Li, T.-K. Sham, L.-M. Liu, G.A. Botton, X. Sun, Platinum single-atom and cluster catalysis of the hydrogen evolution reaction, Nat. Commun. 7 (1) (2016), https://doi.org/10.1038/ncomms13638.